USGS FINAL TECHNICAL REPORT

Award number : G20AP00024

Title:
Shallow rigidity structure from co-located pressure and seismic data and estimation of Vs30 from it

Recipients:
The Regents of the University of California
3227 Cheadle Hall
Santa Barbara, California 93106-2050
Tel (805) 893-7360; fax (805) 893-2611; Email: proposals@research.ucsb.edu

Principal Investigators:
Toshiro Tanimoto and Ralph Archuleta
toshirotanimoto@ucsb.edu, archuleta@ucsb.edu
Earth Research Institute and Department of Earth Science
University of California, Santa Barbara
CA93106

Term of the Award:
January, 2020 – June, 2021 (with 6 months no-cost extension)

Keywords:
Vs30, Shallow elastic structure

Abstract

There are now many sites that are equipped with co-located pressure and seismic sensors. We have developed a new method of estimating Vs30 by analyzing such co-located pressure and seismic data. This method can determine elastic constants, primarily shear modulus, in the uppermost 50-100 m of the crust. After establishing an inversion algorithm, we tested this method for a nine-station array with co-located sensors at Piñon Flat Observatory in Southern California and confirmed that the result for Vs30 is consistent with an independent result by Yong et al. (2016). We then applied this method to the EarthScope TA stations from 2012 to 2018 when all stations were equipped with high-quality infrasound pressure sensors and broadband seismometers. The total number of stations for which we estimated Vs30 became 744. This list for Vs30 is the main contribution of this project. These updated Vs30 should lead to an improved ground-motion predictions at the time of earthquakes.

1.Introduction

There are now many sites that are equipped with co-located pressure and seismic sensors. Examples are the EarthScope Transportable Array (TA) from 2011 to 2018 and other regional US and global networks for which high-quality pressure sensors were installed in the past ten years. These co-located sensors make an ideal set of instruments to examine seismic signals (noise) that is generated by surface pressure changes and the analysis of such signals give us a new way of determining shallow elastic structure for the upper 50-100 m of the Earth. Our goal was to obtain estimates for Vs30 (e.g., Allen and Wald, 2007, 2009; Wald and Allen, 2009) based upon this new approach as Vs30 is a critical feature of most ground motion prediction equations such as NGA West2 (Bozorgnia, 2014) and NGA East (PEER, 2015).

Our approach relies on the fact that we can identify time intervals when surface pressure is the primary source of seismic noise; this can be achieved relatively easily by computing coherence between co-located pressure and seismic data. High coherence between pressure and seismic data for frequencies between about 0.01 Hz and 0.05 Hz has been known since about 1970 (e.g., Sorrells, 1970; McDonald et al., 1971; Sorrells and Goforth, 1973; De Angelis and Boden, 2012; Hutt et al., 2017). Recent data clearly show that when pressure power spectral density (PSD) exceeds about 10 (Pa^2/Hz), high coherence becomes evident at many stations (Tanimoto and Valovcin, 2016). For these highly-coherent time intervals, we are literally observing elastic response of the solid Earth caused by surface pressure changes. Pressure data are the excitation-source signals and seismic data show the resulting elastic response of the solid Earth.

These data contain information on the elasticity of near-surface structure. We developed an inversion method to obtain shallow structure (Tanimoto and Wang, 2019) following the excitation source model by Sorrells (1971). We then tested it and applied to sites with co-located pressure and seismic sensors (Tanimoto and Wang, 2020; Wang and Tanimoto, 2020). Strictly speaking, our inversion results are for depth distribution of shear modulus and bulk modulus, not seismic velocities. Using empirical relations reported by Brocher (2005) and Boore (2016), we convert the elastic moduli to seismic velocities. In this project, we applied our method to the EarthScope TA stations from 2012 to 2018 and made estimates of Vs30 at 744 stations. The results are given in Table 1 and plotted in Figure 11.

In this report we describe the nature of background processes in section 2, theory and data analysis procedures in section 3, and the results for the EarthScope TA data in section 4.

2. Characteristics in Background Processes
(2.1) Scale length
The characteristic length scale of this phenomenon is determined by wavelengths of wind-related, pressure waves. Since wind speed is typically 1-5 m/s, pressure moves on the surface and we refer to it as pressure wave. Its wavelengths at 0.01 Hz are about 100-500 m and those at 0.05 Hz are about 20-100 m. For our analysis, which is between 0.01 and 0.05 Hz, we take 100 m as the representative horizontal scale length for discussion.

The solid earth deforms by this moving surface pressure and it is recorded as seismic noise; since the characteristic horizontal length scale is 100 m, displacements and tilts also occur at about the same length scale. The depth extent of deformation naturally has a similar length scale. More precise numerical calculations of depth sensitivity kernels show that the depth extent becomes typically 50-100 m. At some windy locations, wind speed can be high and the depth extent of deformation could be much larger accordingly.

This length scale also determines what qualifies as "co-located" observations. Separation of pressure and seismic sensors should be much smaller than 100 m, perhaps only up to about a few meters. We can see that the EarthScope TA qualifies which is illustrated in Figure 2. In this set-up, pressure and seismic sensors are in the same vault with pressure sensor sensing surface pressure at about 1.5m to the left connected by an inlet tube (Figure 2). Seismic motions are detected at a depth about 2 m. Locations of pressure measurements and seismic measurements are separated by about 1.5 m in horizontal direction and 2 m in depth direction. This is clearly smaller than 100 m and thus we can regard these data as co-located measurements.
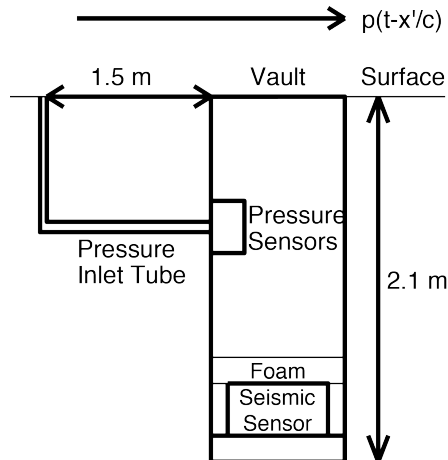
**Figure 2: A typical observational facility of the EarthScope Transportable Array. Seismic sensors are at the bottom of vault at a depth about 2-2.5 m and pressure at the outlet of the inlet tube is measured. Long-period seismic noise (0.01-0.05 Hz) can be explained by wind-related, pressure waves on the surface. We model it by pressure waves that move with wind-like speed (~ 1-10 m/s). They are not related to sound (P) waves.**

(2.2) Coherence and Data Selection

It has been known since about 1970 that co-located seismic and pressure data often show high coherence (> 0.8) between 0.01 Hz and 0.05 Hz. Figure 2 (Left) shows an example of raw coherence values from an EarthScope station KMSC in South Carolina, computed between pressure and vertical seismic displacements. Coherence is plotted as a function of frequency. Such a high coherence between 0.01Hz and 0.05 Hz is commonly observed at many stations. Above 0.05 Hz, the coherence tends to decreases. The right panel (Figure 3) shows the annual average of coherence at the same station plotted against frequency. Generally, the effects of atmospheric pressure, indicated by high coherence, can be traced up to about 0.10-0.12 Hz but it is also clear that the ocean-generated microseisms, especially those due to the primary microseism (0.05Hz-0.07Hz), interfere and reduce coherence values. The arrow in the right panel is given at 0.06 Hz and indicates this interference from ocean-generated seismic signals.

These data suggest that coherence can be used a tool to select data. By selecting time intervals that show high coherence, we are assured that seismic signals are created by local surface pressure variations.
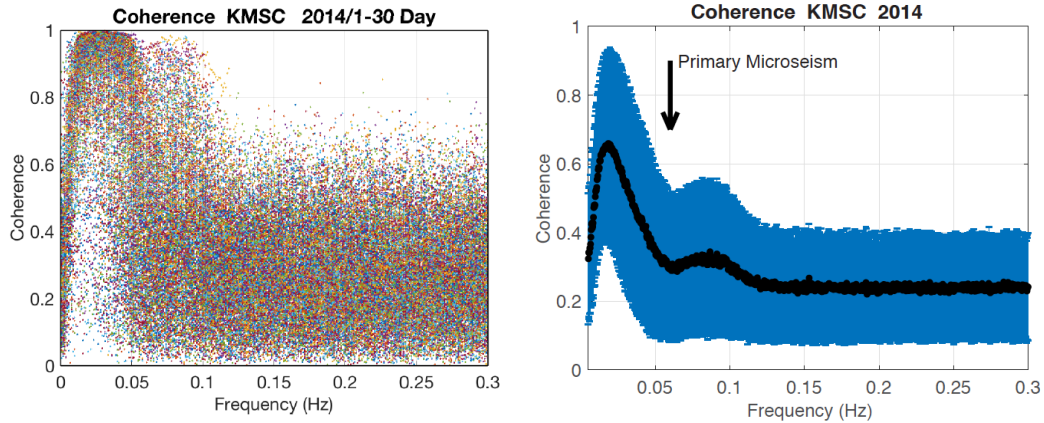
Figure 3: (Left) Raw coherence at station KMSC in South Carolina from the first 30 days in 2014. Coherence between pressure and vertical seismic velocity data was computed for each 1-hour time interval. Different colors are from different 1-hour time series. (Right) The annual average of coherence for the same station in the year 2014. Effects of the ocean-generated microseism weakens the coherence at about 0.06 Hz, but the atmospheric effects can be seen up to about 0.12 Hz.

(2.3) Pressure-Seismic Plot

In order to get an overall picture of pressure and seismic data, we have found it useful to make pressure-seismic plots. Figure 4 (left) shows an example at frequency 0.02 Hz and plots seismic power spectral densities (PSD) against the pressure PSD for this frequency. In this plot, we used pressure and seismic data at KMSC from the entire year of 2014. Each point represents PSDs for one-hour-long time series. Vertical seismic PSDs S_z are plotted in blue and horizontal PSDs (the sum of two directions) S_H are plotted in red. The abscissa is pressure PSD S_p.

Time intervals with high coherence (>0.8) are indicated by green points. Vertical data in the left panel show a near-constant (flat) range (but with large scatter) for the pressure PSD below about

4

1 Pa^2/Hz. It means that the local pressure changes do not influence seismic amplitudes. On the other hand, above about 1 Pa^2/Hz, vertical PSDs become proportional to pressure PSDs; as pressure increases, seismic amplitudes increase. Most high-coherence, one-hour data (green points) are seen above this pressure. This trend in green points suggests that the Earth's surface literally goes up and down with pressure changes (Figure 4, right).

For further quantitative analysis, we measure the gradients $\eta(f) = S_z/S_p$. This parameter $\eta(f)$ is related to the elastic response of the solid Earth. Figure 4 is only for 0.02 Hz but we can see similar features in data between 0.01 Hz and 0.05 Hz. In our approach, we measure $\eta(f)$ between 0.01 Hz and 0.05 Hz. We constructed an inversion algorithm to invert these values for shallow Earth structure.

The ratio of horizontal PSD to pressure PSD, S_H/S_p, also provides similar information to S_z/S_p but when the tilt effects dominate in horizontal data, it provides basically redundant information with vertical seismic data. But its measurement is important because the horizontal to vertical ratios S_H/S_z give us information on pressure-wave speed on surface.
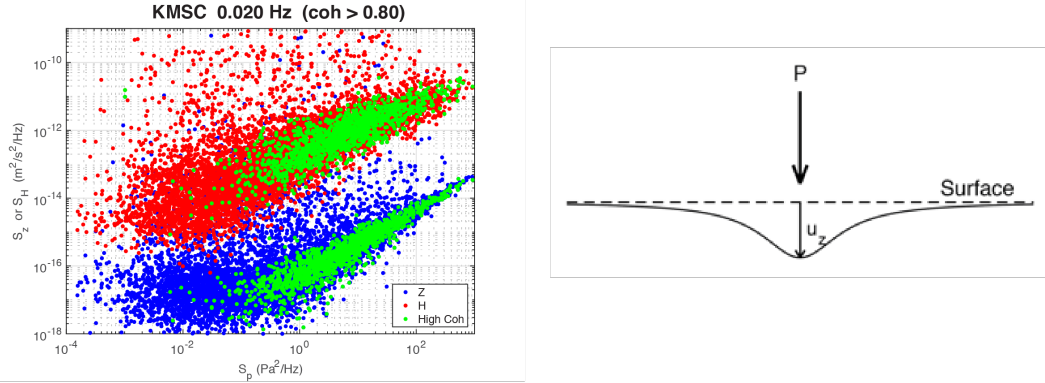
Figure 4: (Left) Seismic velocity PSD plotted against pressure PSD at 0.02 Hz. Vertical PSD in blue and horizontal PSD (sum of two components) in red. (Right) In the high pressure range in the left panel (~10-100 Pa^2/Hz), the solid Earth is basically responding to surface pressure changes.

(2.4) Phase difference between pressure and vertical displacement
We have noted that phase difference between pressure and vertical displacements is ±180 degrees. Figure 5 (bottom) shows examples of phase difference at two stations U54A and U57A (EarthScope TA) in the bottom four panels. The middle panels show plots of coherence plotted against phase differences. The bottom panels show histograms for the same data. They show that when coherence is high (>0.8), phase differences are basically ±180 degrees, meaning that when pressure is high, the Earth's surface is pushed downward and when pressure is low, the surface deforms upward. This can be illustrated by the top panel in Figure 5. It shows that as pressure waves propagate to right (blue wiggle), surface vertical displacements also move to the right with the same speed c but with the opposite sign.

5

"Atmosphere"

p[ω(t-x/c)] : Wind Related Pressure

Sensors   Surface

"Solid Earth"
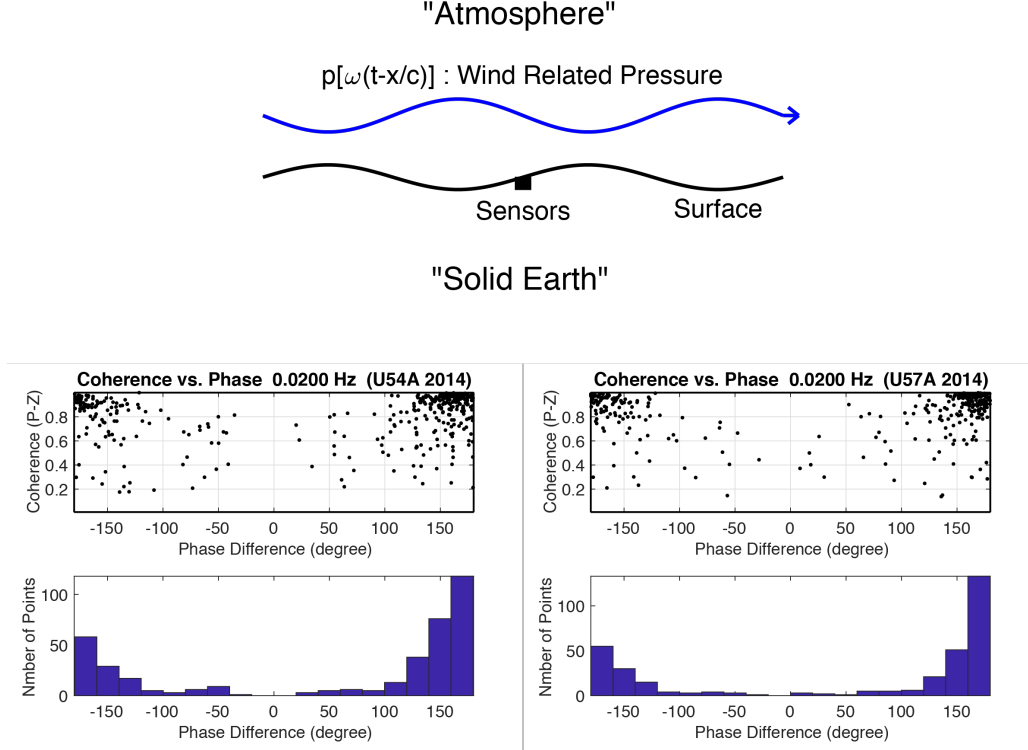
Figure 5: The middle two panels show phase differences between seismic vertical displacement and pressure. Both show that when coherence is high (>0.8), phase differences are close to 180 degrees. Histograms at bottom also support the peaks at about 180 degrees. This can be summarized by a simple picture at top. As pressure wave propagates with speed c, surface deforms with it. When pressure is high, surface is pushed downward and vice versa.

3. Data Analysis and Inversion Algorithm

We describe our inversion algorithm that was developed based on the characteristics summarized in section 2. Our algorithm consists of two main steps. The first step is the measurement of $\eta(f) = S_z/S_p$ and S_H/S_p for frequencies between 0.01 Hz and 0.05 Hz. The second step is the inversion of observed $\eta(f)$ for an underlying structure.

(3.1) Measurement of $\eta(f)$

We take an example from station KMSC to show how our measurements are made. In general, we can write the relationship between S_z and S_p (Tanimoto and Wang, 2018) as

$$S_z(f) = \eta(f)S_p(f) + N_z \qquad (1)$$

where N_z is vertical seismic noise that is independent of local pressure changes. For example, ocean-generated seismic noise is lumped into this term as it is independent of local pressure. This formula suggests that, in the limit of high S_p, $\eta(f)$ can be recovered from the ratio S_z/S_p as

N_z/S_p should become small. Therefore, we select high-coherence data in a high pressure range and take an average of them.

Figure 6 shows an example of this procedure. Green points are from time intervals when coherence was larger than 0.8 and S_p was higher than 10 (Pa²/Hz). We simply take the arithmetic averages of selected green points for our estimates for S_z/S_p and S_H/S_p.

Figure 6 (left) shows a plot of S_z/S_p and S_H/S_p plotted against S_p from the entire year of 2014. As we stated above, we measure S_H/S_p in order to estimate c, the speed of pressure waves on the surface. This parameter is important for the computation of depth sensitivity kernels that are needed in the inversion.

If we changed the cutoff value of coherence (0.8 in Figure 6), the distributions of green points change, In order to check the dependency of our estimates on a choice of the coherence cutoff value, Figure 6 (right) shows our estimates when we varied the coherence cutoff from 0.7 to 0.9 at an interval of 0.05. The top panel shows that our estimates at five frequencies are not affected much from the choice of coherence (as long as it is larger than 0.7), and the bottom panels show how the number of chosen points vary with each choice of coherence cutoff. They indicate that we can make fairly robust estimates for $\eta(f)$ as the estimates are not influenced very much depending on the cutoff values.
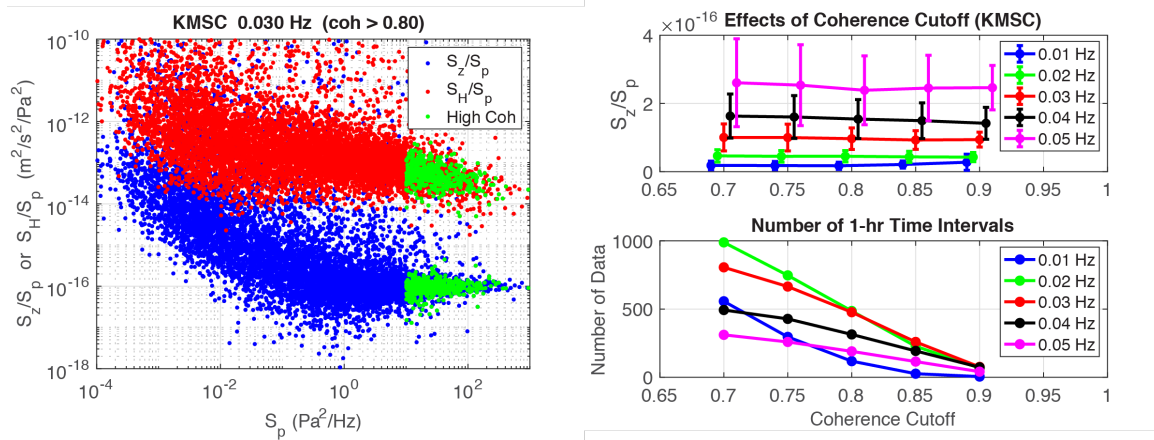
Figure 6: S_z/S_p and S_H/S_p plotted against S_p. Asymptotic values for large S_p give us our estimates of these ratios. Green points indicate the time intervals with coherence higher than 0.8 and pressure PSD is higher than 10 Pa²/Hz. Averaging for green points give us our estimates for the two ratios.

(3.2) Pressure-wave Speed, depth sensitivity kernels and the inversion algorithm
Before describing the inversion algorithm, we discuss two important quantities that are needed for inversion. One is pressure-wave speed on the surface (c) and the other is depth sensitivity kernels. Getting pressure-wave speed is straight-forward. Once we make estimates for S_z/S_p and S_H/S_p, we compute the speed of pressure waves from

$$c^2 = \frac{g^2}{\omega^2} \frac{S_z}{S_H} \tag{2}$$

This speed is needed for an input to the computation of depth resolution kernels.

We developed a program to compute theoretical $\eta(f)$ and its depth sensitivity kernels (Tanimoto and Wang, 2019). We take density (ρ), the bulk modulus (κ) and the shear modulus (the rigidity, μ) as independent parameters. Perturbations to $\eta(f)$ are then related to perturbations of density, bulk modulus and shear modulus and can be expressed by

$$\frac{\delta\eta}{\eta} = \int\{K'_{\rho}\frac{\delta\rho}{\rho} + K_{\kappa}\frac{\delta\kappa}{\kappa} + K_{\mu}\frac{\delta\mu}{\mu}\}\,dz \qquad (3)$$

where K'_{ρ} is the depth sensitivity kernel, K_{κ} is the bulk modulus kernel and K_{μ} is the rigidity kernel.

Figure 7 shows an example of depth sensitivity kernels (two right panels). They were computed for the Model BJ97gr760 by Boore (2016), given in the left panel. The middle panel shows when we took density, P-wave velocity and S-wave velocity as independent parameters. The right panel shows when we took density and two elastic moduli as independent parameters. There is an important difference in density kernels between these two schemes in that the density kernel is essentially zero in the right panel. It means that if we invert for elastic moduli instead of seismic velocities, density essentially does not influence the inversion results. This is related to the fact that deformation of the medium is quasi-static. Using this feature, we perform the inversions only for depth distributions of bulk modulus and shear modulus.
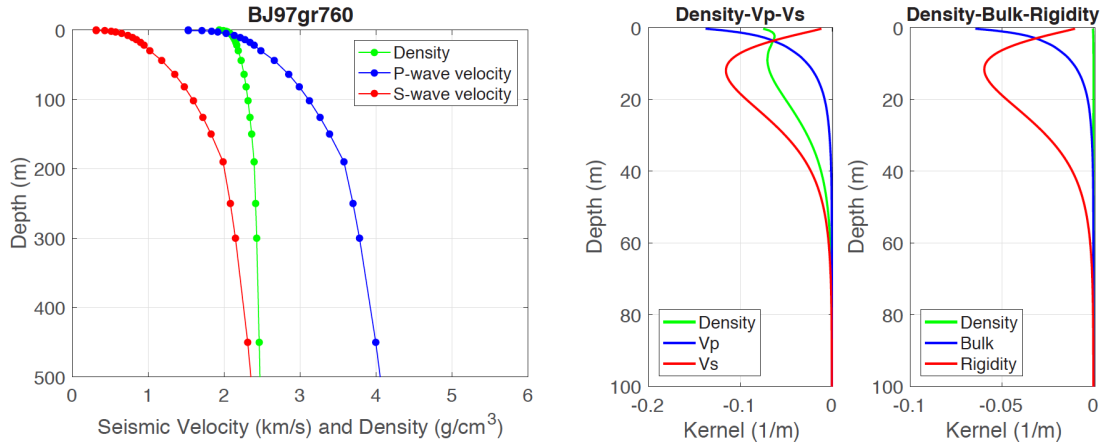
Figure 7: (Left) Model BJ97gr760. (Middle) Depth sensitivity kernels when density, P-wave velocity and S-wave velocity are taken as parameters. (Right) Depth sensitivity kernels when density, bulk modulus, and rigidity are taken as parameters. The density kernel is basically zero in this case.

We constructed the inversion steps based on the following formula (4). Because the density kernels in (3) are small, we drop the density term in (3). Rewriting the left-hand side term in (3) by using $\eta_O(f)$ and $\eta_T(f)$ which are the observed $\eta(f)$ and the theoretical $\eta(f)$, we can write the inversion formula as

$$\frac{\eta_O(f) - \eta_T(f)}{\eta_T(f)} = \int \left\{ K_\kappa \frac{\delta \kappa}{\kappa} + K_\mu \frac{\delta \mu}{\mu} \right\} dz \qquad (4)$$

We replaced $\delta\eta(f)/\eta(f)$ on the left-hand side term in (3) by a combination of the observed value (η_O) and the theoretical value $\eta_T(f)$. Using this formula, we perform a nonlinear, iterative inversion. We construct a starting model by a procedure described in Tanimoto and Wang (2019); for this starting model, we compute its theoretical value $\eta_T(f)$ which in general show some deviations from the observed values. We invert these misfits, computed from the left-hand side of (4) for each frequency, for the depth distributions of the bulk modulus and the rigidity. In this process, we replace the integral on the right-hand side by a sum of contributions from thin homogeneous layers with the same thickness of 0.5 m. In each layer, we assume that density, the bulk modulus and the rigidity are constant. Then we obtain $\delta\kappa$ and $\delta\mu$ for each layer and update the model (structure). We repeat the same procedure until the misfits for $\eta(f)$ become quite small.
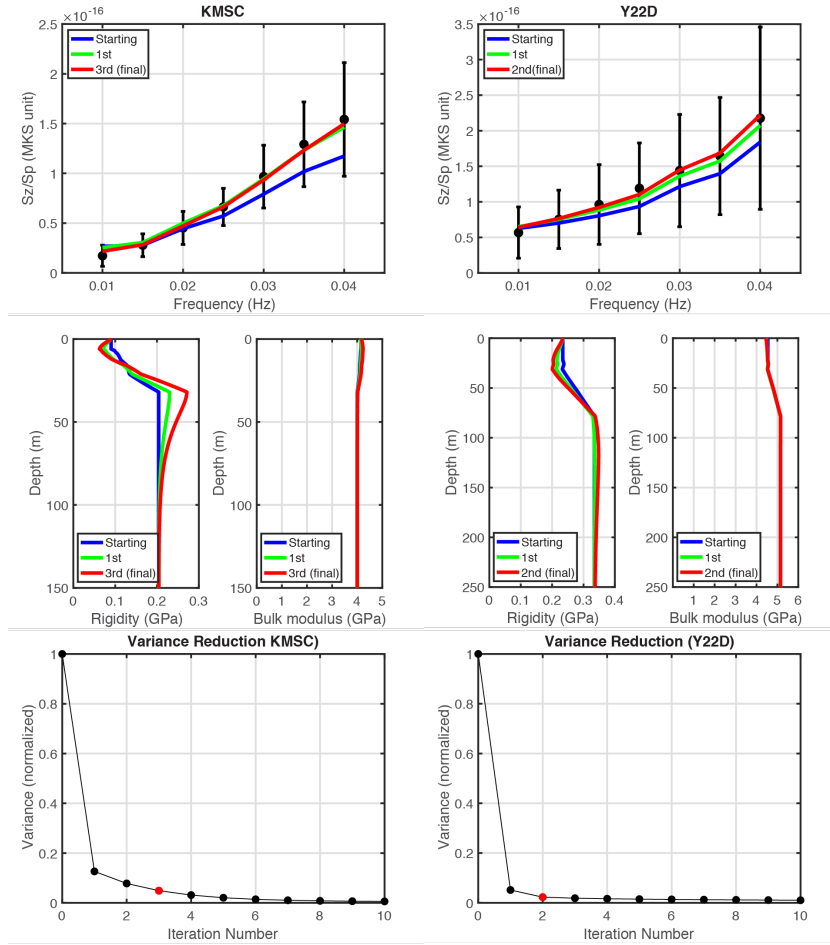
Figure 8: The left panels are the inverted results for KMSC in South Carolina and the right panels are for Y22D is in Socorro, New Mexico. (top)The measured values η(f) at seven frequencies with 1σ error bars. Theoretical η(f) for the starting model is shown by blue lines. Theoretical values for the first and the third iteration are shown in green and red. (middle) Depth distributions of the shear modulus (left) and of the bulk modulus (right). (bottom) Decrease of variance for each step of inversion.

9

By using the sum of misfits from all frequencies we judge the convergence of this nonlinear iterations. Two examples of inversion for stations KMSC and Y22D are shown in Figure 8. The top panels show the observed $\eta(f)$ and its 1σ deviations by the circles and the error bars. Three lines in color show the theoretical values for the starting model (blue), the first iteration model (green) and the final model (red). We stopped the inversion at the third step for KMSC and the second step for Y22D.

In the bottom panels, we show the change of the misfits which decrease rapidly in the first 2 or 3 steps. We typically continue the iterations up to the 10th step but the misfits do not improve very much after the third iteration.

Depth variations of the bulk modulus (left) and the rigidity (right) are shown for each station using the same colors for the iteration steps as in the top panels. The final models indicate that a low rigidity layer is required for KMSC in the upper 20m and also for Y22D in the upper 50m.

Depth sensitivity kernels for each inversion are shown in Figure 9; these kernels are for the starting models of each case. The depth sensitivity kernels can change from iteration to iteration but in practice they remain quite similar throughout the course of inversion.
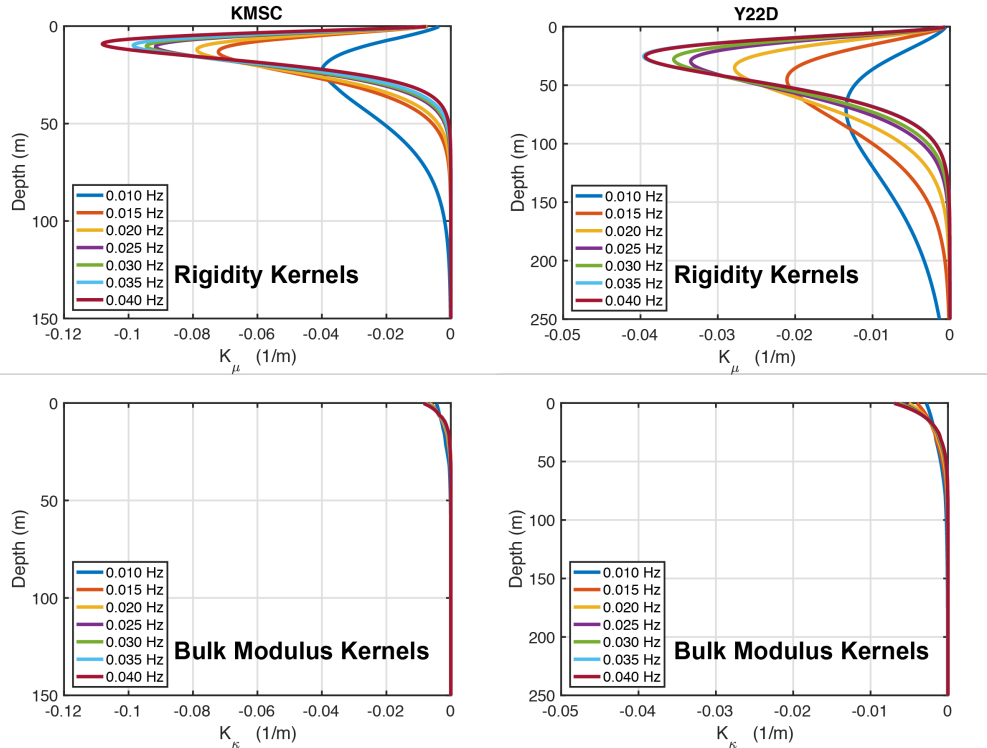
Figure 9: Depth sensitivity kernels for KMSC and Y22D. Depth extent is larger for Y22D because the speed of pressure waves is larger. It is typically 2 m/s for KMSC while it is about 5 m/s for Y22D. Depth extent of sensitivity kernels is proportional to the speed c.

(b)Testing our method using independent measurement of Vs30 at PFO
The Piñon Flat Observatory in southern California (PFO) has a very dense array of co-located stations. We applied our method to nine stations with pressure and seismic sensors and the resulting Vs30 values are shown in Figure 10. The official station names are BPH01 to BPH12 where only the numbers are shown in Figure 10.

Geophone based measurement of Vs30 was obtained by Yong et al. (2016) along the red line in the figure (denoted as USGS). Their Vs30 estimate was between 685 and 840. Our estimate for Vs30 at the closest station (1, BPH01) was 739 (m/s), showing a good agreement. While Vs30 can vary substantially over a distance of about 200-300 m, our results are generally in good agreement with Yong et al. (2016).
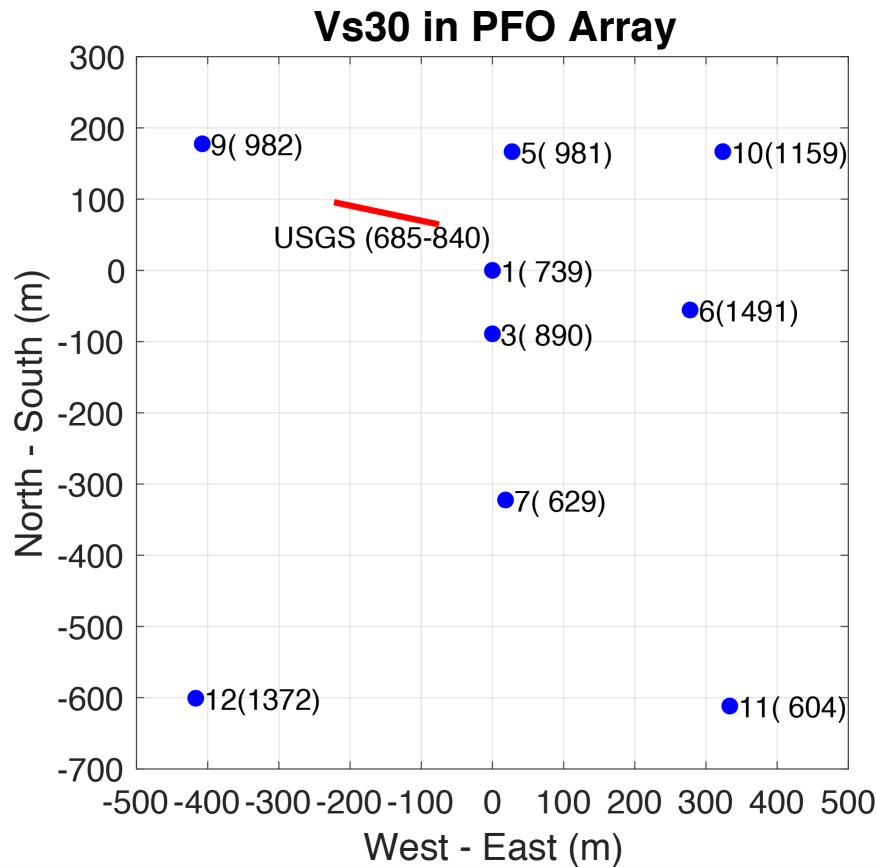
Figure 10: Estimates of Vs30 at nine stations (blue circles) at PFO. Vs30s are shown in parentheses in unit of m/s and the value by Yong et al. (2016) is shown along their linear-array site (red line).

4. Analysis of the EarthScope TA data (2012-2018)

We applied our method to the EarthScope TA data from 2012 to 2018. For pressure data, there is an option to use either infrasound data (Hyperion sensors) or barometer data (Setra 270). In this study, we used the infrasound data because in our preliminary analysis of pressure data, the infrasound data (Hyperion) provided slightly better dynamic range than barometers (Setra 270) for the frequency range from 0.01 Hz to 0.05 Hz.

Figure 11 shows our results for Vs30 at 744 stations for which we could reliably estimate Vs30. Vs30 values are shown by color. Note that the color scale is capped at 1200 m/s (higher values are shown the same color, blue).

While Vs30 could change over a short distance of 200-300 m, we can identify some regional systematics in Figure 11. For example, the area of Mississippi embayment shows particularly low Vs30, indicating an existence of thick sediments in the Mississippi river delta. There is also a generally high Vs30 region that can be traced by green and yellow colors in the northeast region (from NE to SW) which is basically along the Appalachian Mountains.

Comparison of these values for Vs30 against the values in Yong et al. (2016) is shown in Figure 12. All results are shown by three different markers with solid black showing those in the Appalachian Mountains and green markers from the Mississippi embayment. There is clearly large scatter in Figure 12, but there is better agreements in general for smaller Vs30 (< 400 m/s). Such an agreement at low Vs30 values is important as amplification of seismic waves become significant for regions with small Vs30.

Our Vs30 results are also summarized in Table 1. These are essentially the main contribution of this project.
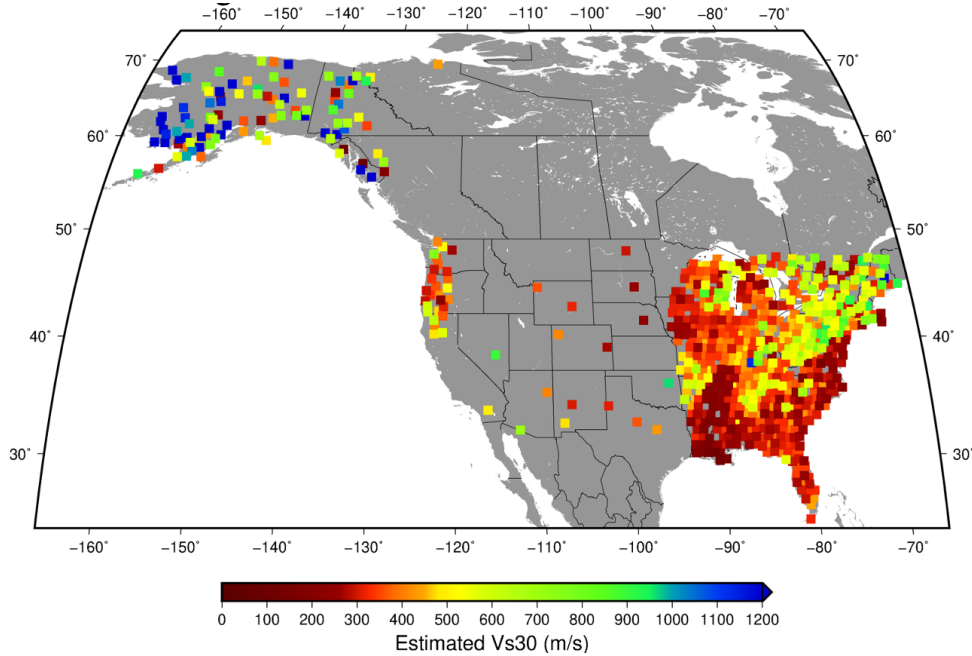
Figure 11: Vs30 estimated by our approach for EarthScope stations 2012-2018. Scale is saturated at 1200 m/s.
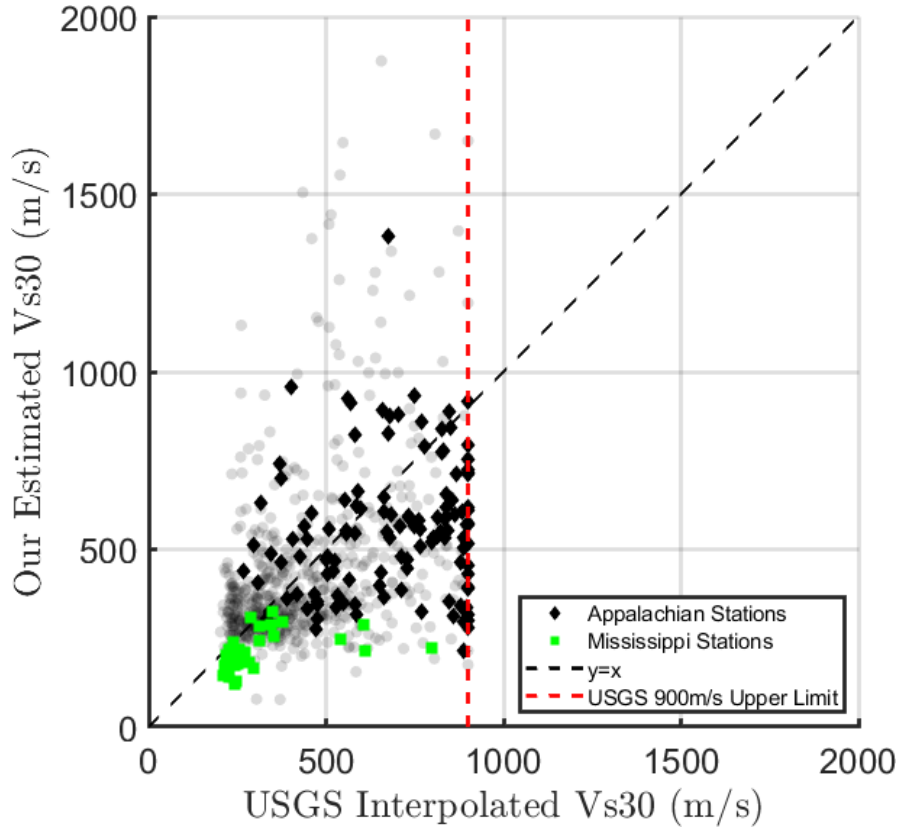
Figure 12: Comparison between our results (the ordinate) and the USGS estimates (the abscissa, Yong et al., 2016). Vs30 by USGS is capped at 900 m/s. Grey shows all stations. In order to show the results for the Mississippi embayment region (green) and the Appalachian mountain region (black), different marks are shown.

BIBLIOGRAPHY OF PUBLICATIONS

Wang, J. and T. Tanimoto (2020), Estimating near-surface rigidity from low-frequency noise using collocated pressure and horizontal seismic data, Bulletin of the Seismological Society of America, XX, 1-11, https://doi.org/10.1785/0120200098

Tanimoto, T. and J. Wang (2020), Shallow elasticity structure from colocated pressure and seismic stations in the Pinyon Flat Observatory and estimation of Vs30, Geophysical Journal International, 222, 678-696. https://doi.org/10.1093/gji/ggaa195

Tanimoto, T. and Yijing Li (2020), Nature of low-frequency, atmosphere generated seismic noise, Journal of Geophysical Research, Solid Earth, 125, e2020JB019423, https://doi.org/10.1029/2020JB019423

Tanimoto, T. and J. Wang (2021), Incorporating wind information in the inversion of co-Located pressure and seismic data for shallow elastic structure, Journal of Geophysical Research, Solid Earth, 126, e2020JB021162. https://doi.org/10.1029/2020JB021162

In addition to these papers, there will be a Ph.D. thesis by Mr. Jiong Wang, planned to be filed in summer, 2021, and a paper to be submitted that describes the analysis for 744 stations.

REFERENCES

Allen, T. I., and D. J. Wald (2007). Topographic slope as a proxy for global seismic site conditions (Vs30) and amplification around the globe, U.S. Geol. Surv. Open-File Rept. 2007-1357, 69 pp.

Allen, T. I., and D. J. Wald (2009). On the use of high-resolution topographic data as a proxy for seismic site conditions (Vs30), Bull. Seismol. Soc. Am. 99, no. 2A, 935–943, doi:10.1785/0120080255.

Boore, D. M. (2016), Determining generic velocity and density models for crustal amplification calculations, with an update of the Boore and Joyner (1997) generic site amplification for Vs(Z)=760 m/s, Bull. Seism. Soc. Am., 106, 316-320, doi:10.1785/0120150229

Boore, D. M. and W. B. Joyner (1997), Site amplifications for generic rock sites, Bull. Seism. Soc. Am., 87, 327-341.

Bozorgnia Y., Abrahamson N.A., Al Atik L., Ancheta T.D., Atkinson G.M., Baker J., Baltay A., Boore D.M, Campbell K.W., Chiou B.-S.J., Darragh R.B., Day S., Donahue J., Graves R.W., Gregor N., Hanks T., IdrissI.M., Kamai R., Kishida T., Kottke A., Mahin S.A., Rezaeian S., Rowshandel B., Seyhan E., Shahi S., Shantz T., Silva W.J., Spudich P., Stewart J.P., Watson-Lamprey J., Wooddell K.E., Youngs R.R. (2014). NGA-West2r esearch project, Earthq. Spectra , 30(3): 973–987.

Brocher, T. M. (2005), Empirical relations between elastic wavespeeds and density in the Earth's crust, Bull. Seism. Soc. Am., 95, 2081-2092, doi10.1785/0120050077

De Angelis, S. and P. Bodin (2012), Watching the wind: Seismic data contamination at long periods due to atmospheric pressure-field-induced tilting. Bull. Seism. Soc. Am., 102, 1255-1265, doi:10.1785/0120110186.

Hutt, C. R., A. Ringler and L. S. Gee (2017), Broadband seismic noise attenuation versus depth at the Albuquerque Seismological Laboratory, Bull. Seism. Soc. Am., 107, doi:10.1785/0120160187.

McDonald, J. A., E. J. Douze, and E. Herrin (1971). The structure of atmospheric turbulence and its application to the design of pipe arrays. Geophys. J. R. Astr. Soc., 26, 99-106.

PEER (2015). NGA-East: Median Ground-Motion Models for the Central and Eastern North America Region, PEER Report No. 2015/04 , Pacific Earthquake Engineering Research Center, University of California, Berkeley, CA

Sorrells, G. (1971), A preliminary investigation into the relationship between long-period seismic noise and local fluctuations in the atmospheric pressure field, Geophys. J. R. Astr. Soc., 26, 71-82.

Sorrells, G. and T. Goforth (1973), Low-frequency earth motion generated by slowly propagating partially organized pressure fields, Bull. Seism. Soc. Am., 63, 1583-1601.

Tanimoto, T. and J. Wang (2018), Low-frequency seismic noise characteristics from the analysis of co-located seismic and pressure data, under review, Journal of Geophysical Research: Solid Earth, 123, 5853-5885. https://doi.org/10.1029/2018JB015519

Tanimoto, T. and J. Wang (2019), Theory for deriving shallow elasticity structure from collocated seismic and pressure data, Journal of Geophysical Research: *Solid Earth, 124*, 5811-5835. https://doi.org/10.1029/2018JB017132

Tanimoto, T. and J. Wang (2020), Shallow elasticity structure from colocated pressure and seismic stations in the Pinyon Flat Observatory and estimation of Vs30, Geophysical Journal International, 222, 678-696. https://doi.org/10.1093/gji/ggaa195

Tanimoto, T. and J. Wang (2021), Incorporating wind information in the inversion of co-Located pressure and seismic data for shallow elastic structure, Journal of Geophysical Research, Solid Earth, 126, e2020JB021162. https://doi.org/10.1029/2020JB021162

Tanimoto, T. & A. Valovcin (2016), Existence of the Threshold Pressure for Seismic Excitation by Atmospheric Disturbances, Geophys. Res. Lett., 43, doi:10.1002/2016GL070858.

Tytell, J., F. Vernon, M. Hedlin, C. de Groot Hedlin, J. Reyes, B. Busby, K. Hafner, and J. Eakins (2016), The USArray transportable array as a platform for weather observation and research, Bull. Am. Meteo. Soc., 97, 603-619, doi:10.1175/BAMS-D-14-00204.1

Wald, D. J., and T. I. Allen (2007). Topographic slope as a proxy for seismic site conditions and amplification, Bull. Seismol. Soc. Am. 97, no. 5, 1379–1395, doi: 10.1785/0120060267.

Wang, J. and T. Tanimoto (2020), Estimating near-surface rigidity from low-frequency noise using collocated pressure and horizontal seismic data, Bulletin of the Seismological Society of America, XX, 1-11, https://doi.org/10.1785/0120200098

Yong, A., E. Thompson, D. Wald, K. Knudsen, J. Odum, W. Stephenson, and S. Haefner (2016). Compilation of Vs30 data for the United States: U. S. Geological Survey Data Series 978, 8p., http://dx.doi.org/10.3133/ds978.

Table 1: Estimates of Vs30 by our method. From left to right, network code, station name, latitude, longitude and Vs30. These results are plotted in Figure 11.

NET	STA	LAT (deg)	LON (deg)	Vs30 (m/s)
TA	058A	27.0569	-81.8049	304.6
TA	059A	26.9671	-81.1440	325.0
TA	059Z	26.3373	-81.4432	291.6
TA	060A	27.0361	-80.3618	326.1
TA	060Z	26.4062	-80.5560	435.1
TA	061Z	25.8657	-80.9070	445.6
TA	062Z	24.7266	-81.0523	321.2
TA	121A	32.5324	-107.7851	477.0
TA	140A	32.6408	-93.5740	205.4
TA	141A	32.6046	-92.9049	303.2
TA	142A	32.5488	-91.9457	210.4
TA	143A	32.7032	-91.4036	181.2
TA	144A	32.6304	-90.4226	199.9
TA	145A	32.6035	-89.9287	241.1
TA	146A	32.6368	-89.0573	284.7
TA	147A	32.6738	-88.2708	524.2
TA	148A	32.6469	-87.5710	280.4
TA	149A	32.5983	-86.7916	284.5
TA	150A	32.6067	-86.0220	362.0
TA	151A	32.5269	-85.3267	361.8
TA	152A	32.6686	-84.7188	290.7
TA	153A	32.6499	-83.8316	337.0
TA	154A	32.6131	-83.1066	325.2
TA	155A	32.6219	-82.4665	432.0
TA	156A	32.6542	-81.4950	269.9
TA	157A	32.6780	-80.9972	309.2
TA	158A	32.7364	-80.1935	303.7
TA	214A	31.9559	-112.8115	710.2
TA	241A	32.0227	-92.9188	278.2
TA	242A	32.0617	-92.1521	186.8
TA	244A	32.0422	-90.6856	293.4
TA	245A	32.0322	-89.8958	336.4
TA	246A	32.0143	-89.1286	194.0
TA	247A	32.0530	-88.6102	267.5
TA	248A	32.0940	-87.7393	272.3
TA	249A	31.9752	-87.1225	364.8
TA	250A	31.9778	-86.2677	313.2

TA	251A	32.0929	-85.4090	291.7
TA	252A	31.9962	-84.7357	265.8
TA	253A	32.0612	-84.1294	279.2
TA	254A	31.9457	-83.2905	337.3
TA	255A	31.9263	-82.4758	388.0
TA	256A	31.9799	-81.8878	345.1
TA	257A	31.9746	-81.0261	248.0
TA	341A	31.3334	-93.1681	325.2
TA	342A	31.3747	-92.3249	296.8
TA	343A	31.2839	-91.6169	145.4
TA	345A	31.3080	-90.0309	288.7
TA	346A	31.3876	-89.4649	276.7
TA	347A	31.4017	-88.5412	257.3
TA	348A	31.4129	-87.9023	281.9
TA	349A	31.3504	-87.1924	281.6
TA	350A	31.4207	-86.3353	270.8
TA	351A	31.2753	-85.6036	322.4
TA	352A	31.4793	-84.9274	289.3
TA	353A	31.3474	-84.2172	375.3
TA	355A	31.3438	-82.8518	322.0
TA	356A	31.3247	-82.1275	277.1
TA	357A	31.4239	-81.4855	264.7
TA	441A	30.7498	-93.1898	237.0
TA	442A	30.7119	-92.4314	188.0
TA	443A	30.7642	-91.7809	167.2
TA	444A	30.7153	-90.7463	256.4
TA	445A	30.7303	-90.3380	309.7
TA	446A	30.7912	-89.3645	251.2
TA	447A	30.7952	-88.6542	262.0
TA	449A	30.7596	-87.2151	251.7
TA	450A	30.8038	-86.5863	303.0
TA	451A	30.6160	-85.7467	301.2
TA	452A	30.8492	-85.1830	405.2
TA	453A	30.8541	-84.3197	276.9
TA	454A	30.7145	-83.6302	308.7
TA	455A	30.7422	-83.0260	336.2
TA	456A	30.7248	-82.0223	312.7
TA	457A	30.6199	-81.5563	272.7
TA	541A	30.0596	-93.1875	173.0
TA	542A	30.1247	-92.5513	174.1
TA	543A	30.0856	-91.8557	139.6

TA	544A	30.1100	-91.1612	120.1
TA	545A	30.0441	-90.4894	177.9
TA	552A	30.1327	-85.2938	346.6
TA	553A	30.1890	-84.4317	295.3
TA	554A	30.0841	-83.6836	393.3
TA	555A	30.1212	-82.9666	321.4
TA	556A	30.0015	-82.4057	354.1
TA	557A	30.0160	-81.7291	352.6
TA	645A	29.4573	-90.5966	128.8
TA	646A	29.5832	-89.8245	134.7
TA	655A	29.5107	-83.2552	565.1
TA	656A	29.3689	-82.5348	292.7
TA	657A	29.5852	-81.8665	296.8
TA	658A	29.4220	-81.2578	259.7
TA	757A	28.9413	-82.0685	351.1
TA	758A	28.9621	-81.1996	341.8
TA	857A	28.2670	-82.2291	343.4
TA	858A	28.2126	-81.3616	246.9
TA	859A	28.0592	-80.8984	313.3
TA	957A	27.6702	-82.2357	274.1
TA	958A	27.5855	-81.7543	409.1
TA	959A	27.5240	-80.8791	283.6
TA	A04D	48.7201	-122.7063	405.4
TA	ABTX	32.6238	-99.6431	360.9
TA	B05D	48.2641	-122.0960	519.1
TA	BGNE	41.4083	-98.1502	228.2
TA	C06D	47.9229	-120.8943	267.6
TA	C17K	68.4753	-163.1776	1374.9
TA	C23K	69.8360	-150.6126	651.5
TA	C24K	69.7200	-148.7009	382.6
TA	C36M	69.3475	-124.0703	437.0
TA	D03D	47.5347	-123.0894	752.0
TA	D04E	47.1786	-122.7715	369.3
TA	D25K	69.3220	-146.3751	1259.1
TA	D41A	47.0605	-88.5657	397.5
TA	D46A	46.8910	-84.0357	353.4
TA	D47A	47.0558	-83.1038	603.6
TA	D49A	47.2726	-81.3562	312.2
TA	D51A	47.0904	-79.3733	479.1
TA	D52A	46.9764	-78.4117	640.6
TA	D54A	47.1520	-76.6570	773.2

TA	D57A	47.0172	-73.8878	559.8
TA	D59A	47.0073	-71.8358	278.6
TA	D60A	46.9139	-70.9237	932.8
TA	D61A	47.2022	-70.1868	610.6
TA	D62A	47.0819	-69.0501	771.5
TA	D63A	47.0370	-68.1066	791.7
TA	E04D	46.5566	-122.5673	371.4
TA	E17K	67.0820	-161.8262	2320.0
TA	E18K	67.4213	-160.6027	997.4
TA	E20K	68.2575	-156.1885	847.4
TA	E38A	46.6058	-91.5542	340.7
TA	E39A	46.3777	-90.5557	492.6
TA	E40A	46.4446	-89.8991	470.5
TA	E41A	46.4643	-88.9636	359.6
TA	E42A	46.4301	-87.9140	546.4
TA	E43A	46.3758	-86.9954	571.4
TA	E44A	46.6199	-85.9214	245.9
TA	E45A	46.3563	-85.1774	284.4
TA	E46A	46.3665	-84.3062	420.4
TA	E48A	46.4809	-82.1653	314.7
TA	E50A	46.4232	-80.7378	364.6
TA	E51A	46.5333	-79.4924	783.3
TA	E53A	46.3784	-77.6638	617.8
TA	E55A	46.4538	-76.0572	273.3
TA	E57A	46.4117	-74.1471	648.6
TA	E58A	46.3721	-73.2771	640.6
TA	E59A	46.4803	-72.5108	239.6
TA	E63A	46.4220	-68.4623	887.6
TA	EPYK	66.3701	-136.7191	392.2
TA	F04D	46.0829	-123.0108	292.7
TA	F05D	45.8852	-121.4597	306.6
TA	F24K	67.5187	-147.8871	757.1
TA	F28M	67.6136	-139.8717	720.6
TA	F30M	67.6106	-135.7863	678.1
TA	F31M	67.4410	-133.7420	495.6
TA	F37A	45.7243	-92.6264	330.4
TA	F38A	45.9588	-91.8775	320.6
TA	F39A	45.9153	-90.9190	356.1
TA	F40A	45.9190	-90.1217	369.9
TA	F41A	45.7387	-89.1046	336.7
TA	F42A	45.7587	-88.1347	247.8

TA	F44A	45.9737	-86.4226	554.9
TA	F45A	45.6837	-85.5156	524.1
TA	F46A	45.7737	-84.7586	520.9
TA	F48A	45.8278	-82.6185	581.7
TA	F49A	45.7627	-82.0423	613.5
TA	F51A	45.9284	-79.9150	589.4
TA	F52A	45.7951	-79.3227	338.2
TA	F55A	45.8338	-76.3510	290.0
TA	F57A	45.8122	-74.6928	220.5
TA	F59A	45.8513	-72.7833	270.5
TA	F60A	45.9688	-71.9514	455.8
TA	F61A	45.9743	-70.9921	563.6
TA	F62A	45.8968	-69.9664	384.5
TA	F63A	45.7030	-69.1029	606.5
TA	G03D	45.2115	-123.2641	334.6
TA	G05D	45.2422	-121.3167	373.1
TA	G19K	66.1434	-157.0870	735.0
TA	G21K	66.5156	-153.5058	1442.0
TA	G22K	66.9214	-151.5073	461.9
TA	G25K	66.7653	-146.1013	360.8
TA	G29M	66.9116	-138.0223	1029.3
TA	G30M	66.9808	-136.2216	1279.6
TA	G31M	66.9227	-134.2708	934.3
TA	G38A	45.1693	-91.8549	397.4
TA	G39A	45.2867	-91.1698	381.5
TA	G40A	45.2684	-90.2006	423.3
TA	G41A	45.2118	-89.1816	298.8
TA	G42A	45.2418	-88.4277	370.2
TA	G43A	45.2572	-87.6861	606.6
TA	G45A	45.0404	-85.6571	508.6
TA	G46A	45.3176	-84.8621	244.6
TA	G47A	45.1730	-83.8551	379.2
TA	G53A	45.1222	-78.6237	382.2
TA	G54A	45.3979	-78.0898	640.6
TA	G55A	45.2532	-76.7187	590.3
TA	G57A	45.1036	-74.9855	541.3
TA	G58A	45.1492	-74.0540	286.8
TA	G60A	45.0977	-72.3337	614.2
TA	G61A	45.2827	-71.5273	876.5
TA	G64A	45.2527	-68.7558	1381.0
TA	H04D	44.5234	-122.7377	359.2

TA	H17A	44.3951	-110.5762	358.3
TA	H19K	65.5276	-156.4494	532.7
TA	H20K	65.4924	-154.8808	2357.5
TA	H23K	65.8251	-149.5432	960.6
TA	H38A	44.6753	-92.2820	424.9
TA	H39A	44.6797	-91.2833	264.4
TA	H40A	44.6220	-90.3905	537.8
TA	H42A	44.5091	-88.5311	281.3
TA	H43A	44.4697	-87.7704	613.0
TA	H45A	44.6232	-86.0440	271.1
TA	H46A	44.5397	-85.2034	338.5
TA	H47A	44.5994	-84.2062	264.5
TA	H48A	44.7006	-83.3249	216.2
TA	H52A	44.6422	-79.8888	350.9
TA	H53A	44.5736	-78.5832	617.6
TA	H55A	44.5505	-77.1830	518.8
TA	H56A	44.5930	-76.2594	340.0
TA	H59A	44.6455	-73.6905	616.8
TA	H60A	44.5606	-72.6986	428.6
TA	H62A	44.5743	-71.1559	543.5
TA	H63A	44.6616	-70.0353	305.6
TA	H64A	44.6412	-69.2203	857.4
TA	H65A	44.6961	-68.2469	338.1
TA	H66A	44.7859	-67.3115	923.3
TA	HARP	62.3987	-145.1568	759.9
TA	HDA	64.4091	-146.9482	392.8
TA	I02D	44.1059	-123.8469	294.6
TA	I02E	44.1077	-123.8473	447.0
TA	I03D	43.6972	-123.3487	336.0
TA	I04A	43.7941	-122.4113	418.7
TA	I05D	44.3386	-121.3395	520.8
TA	I20K	64.7962	-154.4783	257.7
TA	I21K	65.1800	-151.9822	543.3
TA	I23K	65.1479	-149.3603	722.1
TA	I26K	65.3064	-143.1541	547.6
TA	I29M	65.3609	-138.3063	257.0
TA	I30M	65.2225	-136.3767	812.6
TA	I36A	44.0191	-94.0143	286.6
TA	I37A	44.0148	-93.4003	306.4
TA	I39A	43.8543	-91.5231	358.4
TA	I40A	43.8916	-90.6177	876.6

TA	I41A	44.0592	-89.8697	307.5
TA	I42A	43.8908	-88.9134	791.8
TA	I43A	43.8844	-88.1460	746.3
TA	I45A	44.0361	-86.2348	281.6
TA	I46A	43.9411	-85.4472	326.4
TA	I47A	44.0193	-84.5096	427.4
TA	I48A	44.1873	-83.7022	316.2
TA	I49A	43.9400	-82.8246	557.1
TA	I51A	43.8036	-81.0231	539.5
TA	I52A	44.0680	-80.1770	347.1
TA	I53A	43.8238	-79.5912	382.5
TA	I55A	44.2161	-77.6817	715.3
TA	I57A	43.9377	-75.6599	647.1
TA	I58A	43.6901	-74.9733	298.1
TA	I59A	43.7957	-73.8744	514.9
TA	I62A	43.8743	-71.3359	587.5
TA	I63A	44.0505	-70.5809	548.1
TA	I64A	43.9197	-69.6347	373.8
TA	J01D	43.1614	-123.9314	336.2
TA	J01E	43.1615	-123.9314	290.2
TA	J04D	43.2405	-122.1093	222.4
TA	J05D	43.2848	-121.2347	407.4
TA	J17K	63.3965	-159.0777	1125.3
TA	J19K	63.9940	-155.6214	1048.6
TA	J20K	64.1767	-154.1467	1153.0
TA	J25K	64.6130	-145.3697	1229.1
TA	J29M	64.4530	-138.2158	347.1
TA	J29N	64.4525	-138.2164	348.4
TA	J36A	43.3292	-94.3395	304.7
TA	J37A	43.3103	-93.5527	251.1
TA	J38A	43.3190	-92.4755	295.3
TA	J40A	43.3965	-90.7406	393.2
TA	J41A	43.3655	-90.0137	342.9
TA	J42A	43.3179	-89.1234	704.6
TA	J43A	43.3808	-88.4185	830.8
TA	J45A	43.4354	-86.3889	295.6
TA	J46A	43.3478	-85.6466	289.1
TA	J47A	43.2382	-84.8214	387.4
TA	J48A	43.2986	-83.7849	400.6
TA	J49A	43.3600	-83.1389	363.6
TA	J52A	43.2407	-80.4764	538.2

TA	J54A	43.2728	-78.6392	368.6
TA	J55A	43.2657	-77.8167	490.7
TA	J57A	43.4099	-75.9968	547.0
TA	J59A	43.4647	-74.5041	602.3
TA	J60A	43.2438	-73.4212	913.4
TA	J62A	43.2262	-71.8127	502.8
TA	K02D	42.6955	-123.6654	599.6
TA	K04D	42.6246	-121.7535	310.8
TA	K15K	62.2938	-161.5308	1554.0
TA	K22A	42.6507	-106.5240	317.1
TA	K24K	63.8036	-145.7784	645.7
TA	K29M	63.8433	-137.5201	1038.7
TA	K36A	42.6381	-94.4507	314.9
TA	K37A	42.7669	-93.6388	316.1
TA	K38A	42.6472	-92.7709	315.0
TA	K39A	42.7050	-91.8878	310.3
TA	K40A	42.6999	-91.1383	412.6
TA	K41A	42.6071	-90.3046	598.2
TA	K42A	42.7792	-89.3457	390.5
TA	K43A	42.7044	-88.3320	558.7
TA	K46A	42.6864	-85.7834	416.5
TA	K48A	42.8032	-84.1197	364.1
TA	K49A	42.7835	-83.4556	411.1
TA	K50A	42.7749	-82.6231	261.6
TA	K51A	42.7223	-81.5082	296.2
TA	K52A	42.7805	-80.7139	327.0
TA	K54A	42.6097	-78.6908	619.8
TA	K55A	42.7278	-78.0696	698.1
TA	K56A	42.6981	-77.3244	533.0
TA	K57A	42.7313	-76.5163	597.2
TA	K58A	42.7633	-75.6473	543.1
TA	K59A	42.7750	-74.8525	838.9
TA	K60A	42.6168	-73.8886	304.7
TA	K61A	42.6695	-73.2676	278.0
TA	K62A	42.6651	-72.2345	596.7
TA	K63A	42.6888	-71.5283	940.0
TA	KMSC	35.1420	-81.3333	242.1
TA	KSCO	39.0112	-102.6273	272.2
TA	L02D	42.1578	-123.6031	584.9
TA	L04D	42.2180	-122.3046	471.5
TA	L15K	61.6780	-161.4869	1669.1

TA	L17K	62.1344	-158.2972	1141.7
TA	L19K	62.1816	-154.8543	797.1
TA	L20K	62.4787	-153.8798	238.0
TA	L26K	63.0254	-143.3478	349.2
TA	L27K	63.0618	-141.8275	715.8
TA	L29M	63.1090	-138.1290	870.0
TA	L36A	42.1009	-94.6676	313.0
TA	L37A	42.1246	-93.7546	328.4
TA	L39A	42.1234	-92.0007	316.4
TA	L40A	42.0628	-91.2218	346.0
TA	L41A	42.0751	-90.4977	359.8
TA	L42A	42.0040	-89.6670	337.4
TA	L43A	42.1833	-88.7423	431.1
TA	L44A	42.1782	-87.9119	364.8
TA	L47A	41.9756	-85.2021	316.9
TA	L48A	41.9438	-84.4329	460.8
TA	L49A	42.1088	-83.7672	396.7
TA	L50A	42.0430	-82.8095	450.0
TA	L53A	41.9539	-80.2598	399.2
TA	L55A	42.1831	-78.4368	564.6
TA	L56A	42.1365	-77.5591	567.7
TA	L57A	42.0005	-76.8492	714.2
TA	L58A	42.0447	-75.8502	713.5
TA	L59A	42.1902	-75.0426	315.4
TA	L60A	41.9890	-74.2226	754.7
TA	L61A	42.1934	-73.5543	570.8
TA	L61B	42.4498	-72.6802	654.5
TA	L62A	42.0328	-72.6617	274.8
TA	L63A	41.8631	-71.6095	481.1
TA	L64A	41.9359	-70.8391	352.5
TA	L65A	42.0295	-70.0528	236.6
TA	M02C	41.3920	-122.8538	641.1
TA	M04C	41.7826	-121.8393	364.0
TA	M15K	60.6947	-160.6884	1645.2
TA	M17K	61.4009	-157.4375	993.8
TA	M19K	61.9037	-154.3915	575.9
TA	M22K	61.7531	-150.1205	359.6
TA	M23K	61.7929	-147.7262	250.4
TA	M24K	62.1067	-146.1750	452.2
TA	M26K	62.4013	-142.9963	799.1
TA	M27K	62.3579	-141.8780	2136.4

TA	M31M	62.2024	-134.3906	546.3
TA	M37A	41.4028	-94.0575	267.8
TA	M38A	41.4175	-93.1965	306.5
TA	M39A	41.4786	-92.1725	286.8
TA	M40A	41.4060	-91.5121	309.1
TA	M41A	41.3750	-90.5422	309.8
TA	M42A	41.4546	-89.7581	291.8
TA	M43A	41.4365	-88.9581	278.8
TA	M44A	41.3882	-88.0432	358.8
TA	M45A	41.3881	-87.2504	307.4
TA	M46A	41.4079	-86.3524	333.4
TA	M47A	41.3594	-85.6214	351.5
TA	M48A	41.4846	-84.7171	394.9
TA	M49A	41.4745	-83.9752	363.6
TA	M50A	41.4035	-83.0428	317.7
TA	M51A	41.3321	-82.1831	394.0
TA	M53A	41.4393	-80.6750	466.2
TA	M54A	41.5079	-79.6647	536.9
TA	M55A	41.4686	-78.7649	407.5
TA	M57A	41.3372	-77.1280	454.3
TA	M58A	41.3721	-76.4603	577.1
TA	M59A	41.5413	-75.4321	511.0
TA	M60A	41.3265	-74.6250	878.9
TA	M61A	41.3104	-73.7673	438.4
TA	M62A	41.4423	-72.8939	467.7
TA	M63A	41.4038	-72.0464	777.2
TA	M64A	41.5509	-71.2102	741.1
TA	M65A	41.5620	-70.6466	155.4
TA	M66A	41.2590	-70.1353	235.9
TA	MDND	47.8481	-99.6029	293.0
TA	MSTX	33.9696	-102.7724	310.2
TA	N02D	40.9740	-122.7050	406.3
TA	N15K	60.1686	-160.0921	1139.6
TA	N16K	60.4742	-158.7690	997.7
TA	N19K	60.8132	-154.4838	3172.7
TA	N20K	61.2001	-152.2089	1650.3
TA	N30M	61.4593	-137.0885	723.2
TA	N31M	61.4862	-135.7796	652.7
TA	N32M	61.1512	-133.0818	345.9
TA	N36A	40.8156	-94.9604	269.6
TA	N37A	40.7582	-94.2095	262.8

TA	N38A	40.7931	-93.2350	263.3
TA	N39A	40.8776	-92.5023	337.6
TA	N40A	40.8841	-91.5837	315.0
TA	N41A	40.7077	-90.8552	349.6
TA	N42A	40.8290	-90.0345	313.8
TA	N43A	40.9394	-89.1735	361.8
TA	N44A	40.7953	-88.1333	323.8
TA	N45A	40.8479	-87.5118	346.9
TA	N46A	40.8949	-86.7352	385.3
TA	N47A	40.8801	-85.6942	414.3
TA	N48A	40.8591	-85.0271	448.2
TA	N49A	40.9220	-84.1825	712.3
TA	N50A	40.7711	-83.1486	453.7
TA	N52A	40.8125	-81.6876	359.9
TA	N53A	40.8065	-80.8377	463.2
TA	N54A	40.9617	-79.9892	439.4
TA	N55A	40.7808	-78.9862	581.9
TA	N56A	40.9171	-78.2953	447.6
TA	N57A	40.7556	-77.5509	393.0
TA	N58A	40.8396	-76.7158	955.5
TA	N59A	40.9168	-75.7703	533.2
TA	N60A	40.8704	-75.1000	825.5
TA	N61A	40.7519	-74.2969	477.6
TA	N62A	40.9313	-73.4677	381.4
TA	N63A	40.9878	-72.5206	231.1
TA	O02D	40.1766	-122.7884	478.5
TA	O03D	40.2947	-121.8018	508.8
TA	O03E	40.2946	-121.8021	569.0
TA	O14K	59.2533	-161.2638	1505.0
TA	O15K	59.1767	-159.8246	1875.1
TA	O16K	59.5938	-158.0932	2014.8
TA	O17K	59.7733	-157.0946	2301.1
TA	O18K	59.8542	-155.2080	2624.2
TA	O19K	60.1952	-154.3201	434.1
TA	O20A	40.1348	-108.2416	410.8
TA	O20K	60.0815	-152.6240	1396.7
TA	O22K	60.4814	-149.7241	428.3
TA	O29M	60.3024	-138.5755	1280.9
TA	O30N	60.7704	-136.0906	1076.1
TA	O37A	40.1664	-94.1461	256.0
TA	O38A	40.1215	-93.4731	265.0

TA	O39A	40.2544	-92.5438	271.3
TA	O40A	40.1212	-91.8740	388.0
TA	O41A	40.1156	-90.8820	366.7
TA	O42A	40.1956	-90.0812	266.0
TA	O43A	40.2856	-89.3130	341.8
TA	O44A	40.1526	-88.4671	356.2
TA	O45A	40.2489	-87.7244	323.6
TA	O47A	40.2361	-86.1742	402.4
TA	O48A	40.2571	-85.1553	368.4
TA	O48B	40.2571	-85.1553	393.2
TA	O50A	40.1468	-83.6199	465.7
TA	O52A	40.1158	-81.8361	473.4
TA	O53A	40.2493	-81.2129	518.7
TA	O54A	40.1821	-80.3778	399.7
TA	O55A	40.2076	-79.3041	546.1
TA	O56A	40.2683	-78.5663	724.8
TA	O57A	40.2104	-77.6354	916.0
TA	O58A	40.1231	-76.9228	844.8
TA	O59A	40.3114	-76.1859	588.5
TA	O60A	40.3177	-75.4050	823.6
TA	O61A	40.0934	-74.5530	325.8
TA	P16K	59.0314	-157.9906	268.3
TA	P17K	59.1953	-156.4394	588.6
TA	P18K	59.3922	-155.2292	479.2
TA	P19K	59.6524	-153.2319	770.8
TA	P23K	59.9979	-147.4031	679.5
TA	P29M	59.6304	-137.7381	653.3
TA	P30M	60.1218	-136.9598	1415.5
TA	P37A	39.5882	-94.3491	368.2
TA	P39B	39.4876	-92.7541	337.9
TA	P40A	39.5299	-92.0483	361.7
TA	P41A	39.6750	-91.0619	460.2
TA	P42A	39.5853	-90.3443	332.3
TA	P43A	39.6409	-89.5213	424.5
TA	P44A	39.4676	-88.6209	397.0
TA	P45A	39.5277	-87.7439	398.2
TA	P46A	39.6178	-87.2067	323.7
TA	P47A	39.4869	-86.2699	456.2
TA	P48A	39.4605	-85.4258	326.8
TA	P49A	39.5342	-84.7164	527.3
TA	P50A	39.6086	-83.7988	283.9

TA	P51A	39.4818	-83.0601	370.5
TA	P52A	39.6337	-82.1325	479.6
TA	P53A	39.4868	-81.3896	415.2
TA	P54A	39.6020	-80.4796	661.8
TA	P55A	39.5078	-79.8265	526.8
TA	P56A	39.5044	-78.8386	646.4
TA	P57A	39.4835	-78.0126	375.3
TA	P58A	39.4891	-77.3005	891.5
TA	P59A	39.6101	-76.4327	254.6
TA	P60A	39.8113	-75.6358	430.6
TA	P61A	39.6734	-74.7919	253.3
TA	Q16K	58.6774	-156.6556	400.4
TA	Q17K	58.2637	-155.8865	1028.9
TA	Q18K	58.6484	-155.0086	1193.9
TA	Q19K	58.9287	-153.6446	759.6
TA	Q23K	59.4296	-146.3399	478.2
TA	Q39A	39.0455	-92.9759	326.3
TA	Q40A	38.9946	-92.0748	260.9
TA	Q41A	38.9539	-91.2317	385.7
TA	Q42A	38.9120	-90.5331	304.4
TA	Q43A	38.9410	-89.6991	382.4
TA	Q44A	38.9032	-89.0170	398.2
TA	Q45A	38.8948	-88.1565	297.9
TA	Q46A	39.0231	-87.3575	418.7
TA	Q47A	38.9362	-86.4261	485.5
TA	Q48A	38.9295	-85.7311	336.4
TA	Q49A	39.0050	-84.8956	490.0
TA	Q50A	38.8436	-83.9790	753.1
TA	Q51A	39.0260	-83.3456	604.2
TA	Q52A	38.9622	-82.2669	373.5
TA	Q53A	38.8586	-81.5251	620.5
TA	Q54A	38.9836	-80.8338	554.0
TA	Q55A	38.9952	-80.0812	469.8
TA	Q56A	39.0401	-79.1871	639.4
TA	Q57A	39.0353	-78.4107	792.4
TA	Q58A	38.9413	-77.6820	617.9
TA	Q59A	38.8644	-76.6548	298.3
TA	Q60A	39.0016	-75.8429	264.2
TA	Q61A	38.8799	-75.3256	260.4
TA	R11A	38.3489	-115.5854	896.1
TA	R11B	38.3489	-115.5854	1214.9

TA	R16K	57.5673	-157.5742	561.7
TA	R17K	57.6397	-156.3872	994.6
TA	R18K	57.5665	-154.4524	376.2
TA	R31K	58.4133	-135.7398	78.3
TA	R38A	38.1868	-93.9056	478.4
TA	R39A	38.3138	-93.0383	400.4
TA	R40A	38.2909	-92.2684	314.5
TA	R41A	38.2976	-91.3795	375.7
TA	R42A	38.2804	-90.7944	335.4
TA	R43A	38.2760	-89.9308	334.0
TA	R44A	38.2475	-89.0809	377.4
TA	R45A	38.2926	-88.2812	457.3
TA	R46A	38.2124	-87.5114	493.5
TA	R47A	38.2957	-86.5270	429.7
TA	R48A	38.4001	-85.8714	302.8
TA	R49A	38.2916	-85.1714	729.9
TA	R51A	38.3001	-83.5834	214.4
TA	R53A	38.3307	-81.9522	557.3
TA	R54A	38.1909	-80.9904	521.0
TA	R55A	38.2825	-80.1195	714.7
TA	R56A	38.4071	-79.4031	547.5
TA	R57A	38.2970	-78.5232	465.2
TA	R58B	37.9636	-77.8787	299.0
TA	R59A	38.2005	-77.1164	229.3
TA	R60A	38.2684	-76.5807	297.7
TA	R61A	38.3303	-75.3390	248.5
TA	S12K	55.7030	-162.0610	933.5
TA	S14K	56.2848	-159.5532	300.3
TA	S31K	57.9616	-136.2320	572.8
TA	S34M	57.9128	-131.1312	490.7
TA	S39A	37.6910	-93.3226	528.0
TA	S40A	37.5988	-92.5014	454.1
TA	S41A	37.5877	-91.7458	357.1
TA	S42A	37.7700	-90.7939	346.3
TA	S44A	37.6936	-89.2551	382.2
TA	S45A	37.6774	-88.5804	457.1
TA	S46A	37.6849	-87.7153	492.2
TA	S47A	37.5946	-86.8779	446.0
TA	S48A	37.6574	-86.0569	1130.8
TA	S49A	37.7849	-85.2875	808.0
TA	S50A	37.6790	-84.4003	404.0

TA	S51A	37.6392	-83.5935	526.9
TA	S52A	37.6791	-83.0784	352.4
TA	S53A	37.6815	-82.1264	337.3
TA	S54A	37.7997	-81.3114	509.6
TA	S55A	37.7724	-80.5013	588.9
TA	S56A	37.6771	-79.5662	214.5
TA	S57A	37.7605	-78.9536	313.5
TA	S58A	37.6126	-78.0511	171.3
TA	S59A	37.7620	-77.2942	265.8
TA	S60A	37.7055	-76.6535	247.4
TA	S61A	37.6804	-75.6727	283.8
TA	SFIN	40.3790	-87.0967	478.1
TA	SPMN	45.2246	-92.8037	303.6
TA	SUSD	44.4429	-98.9556	258.3
TA	T33K	56.8144	-132.9524	77.2
TA	T35M	56.9811	-130.2496	716.2
TA	T38A	37.0354	-94.2930	499.2
TA	T39A	37.0241	-93.3774	451.3
TA	T40A	37.1504	-92.5193	675.7
TA	T41A	37.0436	-91.7636	393.9
TA	T42A	37.0301	-91.0927	513.8
TA	T43A	37.0833	-90.2878	352.4
TA	T44A	37.0860	-89.5896	247.8
TA	T45A	37.0196	-88.6447	223.4
TA	T46A	37.0417	-87.8941	323.3
TA	T47A	36.9881	-87.1055	439.7
TA	T48A	37.1094	-86.3943	423.5
TA	T49A	37.1050	-85.5334	369.9
TA	T50A	37.0204	-84.8384	364.6
TA	T51A	36.9655	-83.9454	466.9
TA	T52A	37.1076	-82.9852	348.3
TA	T53A	36.9823	-82.5350	479.7
TA	T56A	37.0288	-80.0311	365.1
TA	T57A	36.9983	-79.2538	348.3
TA	T58A	36.9454	-78.5338	303.9
TA	T60A	37.1397	-76.7349	234.6
TA	TCOL	64.8735	-147.8618	289.6
TA	TIGA	31.4389	-83.5898	297.7
TA	TPFO	33.6060	-116.4544	493.2
TA	TUL1	35.9104	-95.7919	963.5
TA	U33K	56.1146	-133.1210	2055.7

TA	U35K	55.9154	-130.0257	192.5
TA	U39A	36.3823	-93.4805	370.4
TA	U40A	36.3563	-92.8535	509.6
TA	U41A	36.3440	-91.9203	423.6
TA	U42A	36.3514	-91.2383	527.9
TA	U43A	36.3693	-90.4057	216.3
TA	U44A	36.5047	-89.6863	201.8
TA	U45A	36.3481	-88.7635	293.8
TA	U46A	36.3590	-88.1773	270.8
TA	U47A	36.4413	-87.2892	391.3
TA	U48A	36.5107	-86.5402	385.1
TA	U49A	36.5129	-85.7796	458.3
TA	U50A	36.4156	-84.8431	555.1
TA	U51A	36.3786	-84.0165	353.3
TA	U52A	36.3929	-83.3671	297.8
TA	U53A	36.3644	-82.5765	331.6
TA	U54A	36.5209	-81.8204	342.7
TA	U56A	36.3472	-80.3829	175.2
TA	U57A	36.4319	-79.3364	294.4
TA	U58A	36.3944	-78.5493	261.5
TA	U59A	36.3526	-77.7925	299.3
TA	U60A	36.4718	-77.1596	287.7
TA	U61A	36.3319	-76.4464	237.7
TA	V35K	55.3279	-131.6150	1339.3
TA	V39A	35.8389	-93.6450	578.5
TA	V40A	35.8044	-92.8232	609.2
TA	V41A	35.7851	-92.1554	562.9
TA	V42A	35.8060	-91.3900	286.0
TA	V43A	35.7857	-90.5443	226.0
TA	V44A	35.8282	-89.8954	215.3
TA	V45A	35.7403	-88.9591	241.1
TA	V46A	35.8007	-88.1177	526.4
TA	V47A	35.8278	-87.5205	371.0
TA	V48A	35.7400	-86.8219	457.4
TA	V49A	35.7663	-85.9030	379.9
TA	V50A	35.6713	-85.1000	555.9
TA	V51A	35.8033	-84.3511	592.2
TA	V52A	35.8417	-83.5959	566.7
TA	V53A	35.6694	-82.8124	532.1
TA	V54A	35.7771	-81.9478	390.6
TA	V55A	35.8518	-81.2149	365.4

TA	V56A	35.8097	-80.4963	430.9
TA	V57A	35.8875	-79.7758	553.5
TA	V58A	35.7940	-79.1150	319.6
TA	V59A	35.7649	-78.2394	435.8
TA	V60A	35.7650	-77.2629	252.7
TA	V61A	35.7912	-76.5776	308.8
TA	V62A	35.5612	-75.9570	209.5
TA	W18A	35.1181	-109.7357	406.6
TA	W39A	35.1960	-93.7840	460.1
TA	W41B	35.1736	-92.2479	476.6
TA	W42A	35.2732	-91.5224	198.3
TA	W43A	35.0877	-90.7061	223.2
TA	W44A	35.1395	-89.8161	246.8
TA	W45A	35.1568	-89.1860	224.3
TA	W46A	35.1333	-88.3783	333.2
TA	W47A	35.2511	-87.5946	423.7
TA	W48A	35.1386	-86.9333	519.7
TA	W49A	35.1194	-86.2645	489.7
TA	W50A	35.2002	-85.3119	639.0
TA	W51A	35.1606	-84.7599	343.1
TA	W52A	35.0935	-83.9277	325.1
TA	W53A	35.1696	-83.1630	317.6
TA	W54A	35.0857	-82.1859	430.3
TA	W56A	35.1350	-80.5828	682.0
TA	W58A	35.0208	-79.2333	361.0
TA	W59A	35.1673	-78.4430	255.1
TA	W60A	35.0528	-77.7133	284.6
TA	W61A	35.1773	-76.9909	283.8
TA	WHTX	31.9913	-97.4561	429.3
TA	X39A	34.5105	-94.1138	622.3
TA	X40A	34.4873	-92.8342	467.1
TA	X41A	34.4949	-92.5137	325.7
TA	X42A	34.5532	-91.6262	218.4
TA	X43A	34.5180	-90.8812	201.2
TA	X44A	34.4998	-90.1462	244.1
TA	X45A	34.4241	-89.3931	311.1
TA	X46A	34.5564	-88.5844	320.6
TA	X47A	34.5178	-87.8571	487.1
TA	X48A	34.4517	-87.0452	629.2
TA	X49A	34.5126	-86.3260	533.0
TA	X50B	34.4611	-85.6499	434.2

TA	X51A	34.5658	-84.8574	315.3
TA	X52A	34.6032	-83.8938	343.6
TA	X53A	34.5031	-83.3013	226.2
TA	X54A	34.5474	-82.3743	341.4
TA	X55A	34.4701	-81.6336	283.2
TA	X56A	34.4923	-81.0319	239.6
TA	X57A	34.4643	-80.0940	311.7
TA	X58A	34.5548	-79.3388	342.8
TA	X59A	34.5720	-78.6023	268.4
TA	X60A	34.5773	-77.9768	224.5
TA	Y22D	34.0739	-106.9210	307.9
TA	Y22E	34.0742	-106.9208	303.9
TA	Y40A	34.0124	-93.2798	451.6
TA	Y41A	33.8807	-92.6113	282.7
TA	Y43A	33.9121	-90.9285	193.2
TA	Y44A	33.9618	-90.2112	218.7
TA	Y45A	33.8656	-89.5431	206.1
TA	Y46A	33.8828	-88.8577	332.8
TA	Y47A	33.9025	-87.8494	351.9
TA	Y48A	33.9131	-87.1696	514.1
TA	Y49A	33.8577	-86.4119	575.1
TA	Y50A	33.8911	-85.7347	368.1
TA	Y51A	33.8993	-85.0640	296.4
TA	Y52A	33.8640	-84.0626	417.1
TA	Y53A	33.8554	-83.5836	279.8
TA	Y54A	33.8621	-82.6880	580.1
TA	Y55A	33.9375	-81.8581	485.4
TA	Y56A	33.7922	-81.3047	324.0
TA	Y57A	34.0170	-80.3915	296.9
TA	Y58A	33.9057	-79.6665	381.1
TA	Y59A	33.9897	-78.8737	204.6
TA	Y60A	34.0046	-78.2163	366.7
TA	Z40A	33.2584	-93.3995	330.6
TA	Z41A	33.2577	-92.8030	272.1
TA	Z42A	33.2739	-91.9474	289.3
TA	Z43A	33.2100	-91.2441	217.1
TA	Z45A	33.3705	-89.6913	233.7
TA	Z46A	33.1933	-88.9414	330.6
TA	Z47A	33.1990	-88.0696	271.5
TA	Z48A	33.3764	-87.5556	450.9
TA	Z49A	33.1942	-86.5311	391.7

TA	Z50A	33.2540	-85.9226	451.5
TA	Z51A	33.3167	-85.1747	220.4
TA	Z52A	33.1893	-84.4176	290.3
TA	Z53A	33.2801	-83.5713	244.7
TA	Z54A	33.2362	-82.8417	406.6
TA	Z55A	33.2211	-82.1359	276.8
TA	Z56A	33.3253	-81.3687	253.4
TA	Z57A	33.2970	-80.7039	428.2
TA	Z58A	33.3349	-79.8129	345.8
TA	Z59A	33.2414	-79.2780	306.7